The Atmospheric Overturning Induced by Hector the Convector

Thibaut Dauhut, Jean-Pierre Chaboureau, Patrick Mascart, Olivier Pauluis

The Atmospheric Overturning Induced by Hector the Convector

THIBAUT DAUHUT, JEAN-PIERRE CHABOUREAU, AND PATRICK MASCART

Laboratoire d'Aérologie, Université de Toulouse, CNRS, UPS, Toulouse, France

OLIVIER PAULUIS

Courant Institute of Mathematical Sciences, New York University, New York, New York, and Center for Prototype Climate Modeling, New York University Abu Dhabi, Abu Dhabi, United Arab Emirates

(Manuscript received 6 February 2017, in final form 13 July 2017)

ABSTRACT

The overturning of Hector the Convector, a tropical multicellular convective system of northern Australia that regularly overshoots into the stratosphere, is synthesized at the scale of a large-eddy simulation. The isentropic analysis offers the advantage of filtering out the reversible motions due to gravity waves and taking into account the turbulent fluxes that contribute to the vertical transport. Two key circulations are characterized: the troposphere deep overturning and the mass exchange due to the overshoots into the stratosphere. The transition from deep to very deep convection is associated with a change in the diabatic tendency inside the tallest updrafts: the latent heat release due to the formation of a large amount of icy hydrometeors exceeds the loss of energy due to mixing with the drier, colder air of the environment. In agreement with a previous study of Hector examining the properties of its two tallest updrafts, the entrainment rate exhibits a minimum during the very deep convection phase as low as 0.04 km^{-1}. The overturning intensity corroborates the Eulerian computation of the vertical mass flux in the midtroposphere and in the lower stratosphere. It however gives a lower estimate of the flux in the upper troposphere, filtering out the reversible motions, and a larger estimate in the lower troposphere and at the tropopause, where slow vertical motions contribute significantly to the transport.

1. Introduction

Tropical air masses can experience very fast ascent in deep convective clouds from the low levels of the troposphere up to the lower stratosphere. Satellite observations show indeed that 1.3% of tropical convection reaches the base of the tropical tropopause layer (TTL; between 14- and 18-km altitudes), and 0.1% may even penetrate the lower stratosphere (Liu and Zipser 2005). The net impact of deep convection into the composition of the TTL remains, however, uncertain. Very few studies estimate the convective mass flux within the TTL. Values on the order of $10^{-4}\,kg\,m^{-2}\,s^{-1}$ across the base of the TTL (but almost nil aloft) are reported by studies using a cloud-resolving model (Küpper et al. 2004) and satellite data (Gettelman et al. 2002). Such magnitudes in the convective mass flux are obtained at a higher level across the 17-km altitude in the mid-Pacific using tracer data (Dessler 2002), over Brazil using a cloud-resolving model (Chaboureau et al. 2007), and over Hector the Convector, a multicellular thunderstorm over the Tiwi Islands (northern Australia) using a giga-large-eddy simulation (LES; Dauhut et al. 2016). Beyond the small number of studies estimating such convective mass transport, a further uncertainty arises from the way the convective mass transport is obtained in the cloud-resolving modeling studies. The latter is estimated using the Eulerian method, a common approach that integrates the mass flux across an altitude, where the vertical velocity field exceeds a certain threshold. In doing so, small-scale oscillations in vertical velocity are included in the mass flux estimate while not necessarily contributing to the net mass transport.

An alternative to this caveat is the isentropic analysis developed in Pauluis and Mrowiec (2013). The isentropic analysis consists in averaging the properties of thermodynamically similar air parcels. When using the

Corresponding author: Thibaut Dauhut, thibaut.dauhut@aero.obs-mip.fr

DOI: 10.1175/JAS-D-17-0035.1

equivalent potential temperature as an isentropic coordinate, this method allows the warm, moist upward motions to be separated from the cooler, drier downdrafts (Pauluis and Mrowiec 2013; Mrowiec et al. 2015). Pauluis and Mrowiec (2013) apply this method to highlight the tropospheric overturning in an idealized simulation of radiative–convective equilibrium. Mrowiec et al. (2015) apply the same methodology to analyze the characteristics of the upward and downward mass fluxes in a realistic simulation of a tropical mesoscale convective system. In both studies, the isentropic analysis yields a convective mass transport that is significantly lower than the estimate obtained from the standard Eulerian analysis. The difference can be attributed to the fact that oscillatory motions such as gravity waves can be partially included in the convective mass transport under the Eulerian approach but are filtered out by the isentropic analysis (Pauluis and Mrowiec 2013; Mrowiec et al. 2015).

The main purpose of this study is to quantify the atmospheric overturning for a case of very deep convection reaching the stratosphere by using the isentropic analysis. The case of Hector the Convector on 30 November 2005 has been selected. Using simulations performed with horizontal grid spacings ranging from 100 to 1600 m, Dauhut et al. (2015) find that this Hector storm transported around 3000 tons of water into the stratosphere. Dauhut et al. (2016) examine its tallest updrafts in the giga-LES (the 100-m simulation). They show that the development of the convection toward the stratosphere exhibits four successive phases, each lasting 1 h: the congestus, deep, very deep, and mature convection phases. The hydration of the stratosphere is significant during the very deep convection phase only, and it is due to the two tallest updrafts. The dilution of these tallest updrafts with the surrounding air has been quantified by computing the entrainment rate. The entrainment rate of the tallest updrafts is minimal during the very deep convection phase, as low as $0.08\,\mathrm{km}^{-1}$ across the whole troposphere.

The atmospheric overturning is analyzed in this study during the successive phases of Hector the Convector. Special attention is paid to the troposphere–stratosphere exchanges and to the diabatic processes inside the storm. The isentropic analysis is applied to the simulation of Hector with 200-m horizontal grid spacing and 1-min time resolution. The 3D fields of the simulation have been saved every minute in order both to capture the fast development of Hector and to compute isentropic averages over a characteristic time period of 15 min. The 200-m grid spacing has been selected in order to limit the huge data volume that would be examined with output every minute of the giga-LES. Furthermore, the properties of the updrafts differ little between the giga-LES and the 200-m simulation (Dauhut et al. 2015). In the following, the focus is first on the very deep convection phase to illustrate for the first time the isentropic analysis on a convective system that reaches the stratosphere. Then the main circulations within Hector are identified during the successive phases of its development. The competition between the latent heat release and the mixing of the rising parcels with their environment determines the vigor of the convection. It is investigated, and the entrainment rates are calculated for all the parcels of the domain rather than for the tallest updrafts only (Dauhut et al. 2016).

Section 2 describes the setup of the Meso-NH model and the isentropic analysis. Section 3 illustrates the isentropic analysis with the study of the very deep convection phase of Hector and explains the method to obtain the diabatic tendencies. Section 4 compares the successive convective regimes. It describes their overturning, investigates the diabatic tendencies, and shows the evolution of the entrainment rate. Section 5 quantifies the isentropic mass flux by Hector. Section 6 gives the conclusions.

2. Model design and isentropic analysis

a. Meso-NH large-eddy simulation

The nonhydrostatic mesoscale model Meso-NH (Lafore et al. 1998) is set up over a domain of $256 \times 204.8\,\mathrm{km}^2$ covering the Tiwi Islands, 100 km north of Darwin, Australia (Fig. 1). The domain is wide enough so that the edges, with open boundary conditions, do not affect the development of Hector, located above the islands. The top of the domain is set at 25 km, with a sponge layer in the last 3 km that prevents the reflection of gravity waves. The horizontal and vertical grid spacings are 200 and 100 m, respectively, so that the large eddies inside the clouds are resolved (Dauhut et al. 2016). The 256 model levels follow the small orography (80-m-high hills at maximum) and are slightly tightened close to the surface (down to 40-m vertical spacing). The total number of points is 3.37×10^8. The model uses parameterizations for microphysics (a single-moment one including three icy hydrometeor species), turbulence, radiation, and surface exchanges. The reader is referred to Dauhut et al. (2016) for further details on the parameterizations. The heating rates due to the subgrid processes represented by these parameterizations are available as averaged profiles over the analysis domain (shown in Fig. 1) and over the 15-min integration time periods. Over ocean, the sea surface temperature is fixed to 29°C. Over land, the soil temperature and moisture content evolve with time; they are initialized to 30°C and $0.16\,\mathrm{m}^3\,\mathrm{m}^{-3}$, respectively. The atmosphere is homogeneously initialized in temperature,

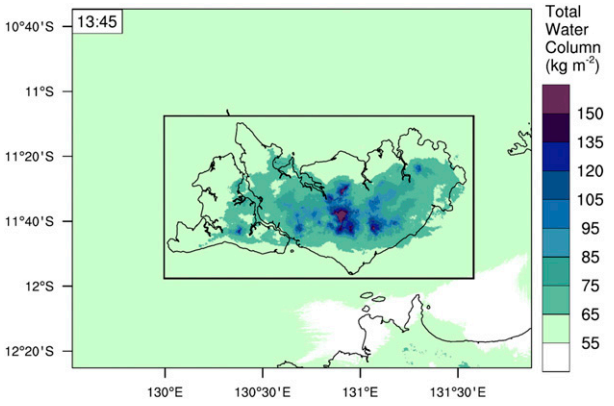

FIG. 1. Domain of simulation. The total water column is shaded. The domain of the isentropic analysis is delimited by the black rectangle. It encompasses an area of 1.6×10^{10} m^2.

humidity, horizontal wind intensity, and direction with the sounding taken in Darwin at 0930 LT (0000 UTC) 30 November 2005.

The sea breeze circulation leads to important convergence of warm, humid air above the surface of the Tiwi Islands during the whole simulation. During the first 2 h, convection develops as cumulus humilis over the islands, then cumulus congestus grow above the convergence lines along the coasts, as in the giga-LES simulation. The cold pools enhance the convergence of humidity at their edges, leading to (from 1230 LT onward) the formation of the cumulonimbus that compose the multicellular system called Hector the Convector. From 1300 LT onward, a couple of updrafts overshoot the tropopause and lead to the injection of cloud particles inside the stratosphere that later on sublimate and hydrate the lower stratosphere (Dauhut et al. 2015). The horizontal extent of Hector at this stage of development, called the very deep convection phase, covers almost the whole Tiwi Islands (Fig. 1).

b. Isentropic analysis

The isentropic analysis gives an overview of the airmass overturning inside the thunderstorm and allows us to compute the irreversible vertical transport by filtering out the oscillatory motions. The technique consists in reducing the four spatiotemporal coordinates into two: a vertical coordinate and an isentropic one, conserved during reversible motions. There is a freedom in the choice of these coordinates. In this study, the vertical coordinate is the altitude z, and the isentropic coordinate is the equivalent potential temperature θ_e. The latter is defined following the formulation of Emanuel (1994):

$$\theta_e = T\left(\frac{p_0}{p}\right)^{R_d/C_p} \exp\left(\frac{L_v r_v}{C_p T}\right) H^{-R_v r_v/C_p}, \qquad (1)$$

where T is the temperature, p_0 is a reference pressure of 1000 hPa, p is the absolute pressure, R_d and R_v are the gas constants for dry air and water vapor, respectively, $C_p = C_{pd} + r_t C_l$ is the specific heat capacity of moist air, C_{pd} is the specific heat capacity of dry air, r_t is the mixing ratio of vapor and liquid water, L_v is the latent heat of vaporization, r_v is the mixing ratio of vapor, and H is the relative humidity. In the frame of moist convection, θ_e gives an insight into the air parcels' capability to rise. However, it is worth noting that warm, dry parcels and cold, moist parcels can share the same θ_e. The exchanges of such parcels are then missed using θ_e, whereas these exchanges may be meaningful. This choice of isentropic coordinate, common to previous studies that apply the isentropic analysis to single convective systems (e.g., Pauluis and Mrowiec 2013; Mrowiec et al. 2015), allows us to compare the results with literature. In section 4b, the use of liquid moist static energy as an alternative isentropic coordinate is discussed.

The equivalent potential temperature θ_e is conserved in a reversible moist adiabatic process. For example, reversible motions like gravity waves do not change air parcels' θ_e. This is also true for the loss or gain of condensed water by precipitation. The equivalent potential temperature θ_e is no longer conserved in the case of phase changes involving ice (freezing, melting, deposition, and sublimation), radiative, and mixing processes.

The reduction of the four spatiotemporal dimensions (x, y, z, t) of a variable field f into the two dimensions (θ_{e0}, z_0) is done with the following integration:

$$\langle f\rangle(\theta_{e0}, z_0) = \frac{1}{PL_xL_y}\int_0^P\int_0^{L_x}\int_0^{L_y} f(x,y,z_0,t) \times \delta[\theta_{e0} - \theta_e(x,y,z_0,t)]\,dy\,dx\,dt, \qquad (2)$$

where P, L_x, and L_y are, respectively, the time period, the zonal extent, and the meridional extent of the isentropic analysis integration (the analysis domain is represented by the black rectangle in Fig. 1); the 0 subscript indicates the coordinates of the isentropic analysis, and δ is the Dirac function (actually approximated here by $1/\Delta\theta_{e0}$ over $[\theta_{e0} - \Delta\theta_{e0}/2, \theta_{e0} + \Delta\theta_{e0}/2]$ and with $\Delta\theta_{e0} = 1$ K). To characterize the overturning, the dynamical, thermodynamical, and microphysical properties of the circulation are conditionally averaged for each (θ_{e0}, z_0) bin, using the following formulation:

$$\tilde{f} = \frac{\langle \rho f\rangle}{\langle \rho\rangle}, \qquad (3)$$

where the tilde indicates the bin average.

Finally, the isentropic streamfunction offers an efficient overview of the airmass overturnings inside the

analysis domain. It is computed by integrating the vertical mass flux from 0 to θ_{e0}, at each level z_0:

$$\Psi(\theta_{e0}, z_0) = \int_0^{\theta_{e0}} \langle \rho w \rangle(\theta'_e, z_0)\, d\theta'_e, \tag{4}$$

where w is the vertical velocity. This method is applied to the 200-m simulation of Hector the Convector. The focus is first on the very deep convection phase in the following section. The different phases of convection are then compared. Finally, the irreversible vertical mass transport is computed.

3. Isentropic analysis of very deep convection

a. Dynamics

The dynamics of Hector are investigated during the very deep convection phase in the frame of the isentropic analysis. The mass distribution, the isentropic vertical mass flux, the isentropic streamfunction, and the conditional average of the vertical velocity are illustrated for a 15-min period during the very deep convection phase in Fig. 2. The environment profile θ_e^{env} together with the 0° and −38°C isotherms are superimposed. The environment profile θ_e^{env} is the constant oceanic profile of the air parcels that enter at the domain edges. The 0° and −38°C isotherms delimit the mixed-phase cloud region, where a significant amount of water changes phase between liquid and solid.

The mass distribution (Fig. 2a) gives the frequency of each θ_e bin at each altitude. The mass distribution is concentrated along the environmental θ_e^{env} profile: more than 90% of the air mass differs from θ_e^{env} by less than 7 K except between 0.9- and 2.8-km altitudes. Air parcels with θ_e higher than 355 K (exceeding the environmental value at the surface) are present but only account for 0.1% of the mass below 13-km altitude.

The isentropic vertical mass flux is shown in Fig. 2b. Below 12.5-km altitude, the vertical mass flux is downward along the θ_e^{env} profile and upward at higher θ_e. The largest contributions to the upward mass flux are due to the updrafts of shallow convection below 3-km altitude ($\theta_e \simeq 353$ K) and to the air parcels with θ_e around 345–350 K in the mixed-phase cloud (between the freezing level and the −38°C isotherm above which virtually no liquid water persists, as shown in Fig. 3e). A large downward mass flux is initiated just below the freezing level, where the cooling from the melting and the sublimation of ice reduces the parcels' buoyancy (visible in Fig. 5 as a local minimum in the θ tendency because of microphysics).

The isentropic streamfunction is shown in Fig. 2c. From a physical point of view, the isentropic streamfunction is equal to the net mass flux at level z of all air parcels with an equivalent potential temperature less than or equal to θ_{e0}. The isentropic streamlines, like the streamlines of an unsteady flow, can be interpreted as the juxtaposition of short Lagrangian paths followed by the air parcels. In contrast with the path of individual air parcels, they are averaged trajectories in the (z, θ_e) space over all the air parcels sharing the same coordinates and over the 15-min time period. The streamfunction is negative below the tropopause, consistent with warm, moist ascent balanced by a subsidence of colder, dryer air. The convective mass transport in this tropospheric overturning reaches a maximum value of 0.15 kg m^{-2} s^{-1} at 4-km altitude. The streamfunction changes sign in the upper troposphere and lower stratosphere, indicative of convective overshoot with cold air rising and warmer air sinking. The mass transport associated with this overshoot overturning is about 0.004 kg m^{-2} s^{-1} across the tropopause.

Among the two overturnings identified during the very deep convection phase, the tropospheric overturning (with negative values in Fig. 2c) is the most intense (with a maximal intensity of 0.15 kg m^{-2} s^{-1}) and the most spatially extended (spanning from the surface to 15-km altitude). From the surface, the ascending branch is made of upright streamlines at high θ_e (350–355 K), indicating a conservation of θ_e along the ascent. The outermost streamline indicates even an increase of θ_e between 2- and 3-km altitudes. This increase might be linked to local numerical effects; its explanation is left to future investigations. At lower θ_e (345–350 K), the upward streamlines are tilted toward lower θ_e values, indicating a decrease of θ_e during the ascent of the air parcels. Among the processes that alter θ_e, the mixing with lower θ_e air parcels is more efficient than the ice melting (effective only from 4-km altitude upward; see the icy hydrometeor loadings in Fig. 3) and the radiative cooling (virtually nil on average up to 10-km altitude; see Fig. 5). In Fig. 2c at the freezing level (around 5 km), the streamlines' discontinuity corresponds to the increase of θ_e due to the latent heat release by ice formation. Between the freezing level and the level of neutral buoyancy (where the streamlines cross the θ_e^{env} profile), the streamlines are upright and the averaged vertical velocities are very large, up to 25 m s^{-1} (Fig. 2d). The constant values of θ_e along the upward streamlines are here due to the fact that the mixing is small (see later section on the entrainment) and to the latent heat release induced by ice formation (Fig. 5). A complementary investigation reveals that the air parcels with θ_e higher than 355 K are part of the strong updrafts (with vertical velocities larger than 10 m s^{-1}) identified by Dauhut et al. (2016). The subsiding branch closely follows the θ_e^{env} profile

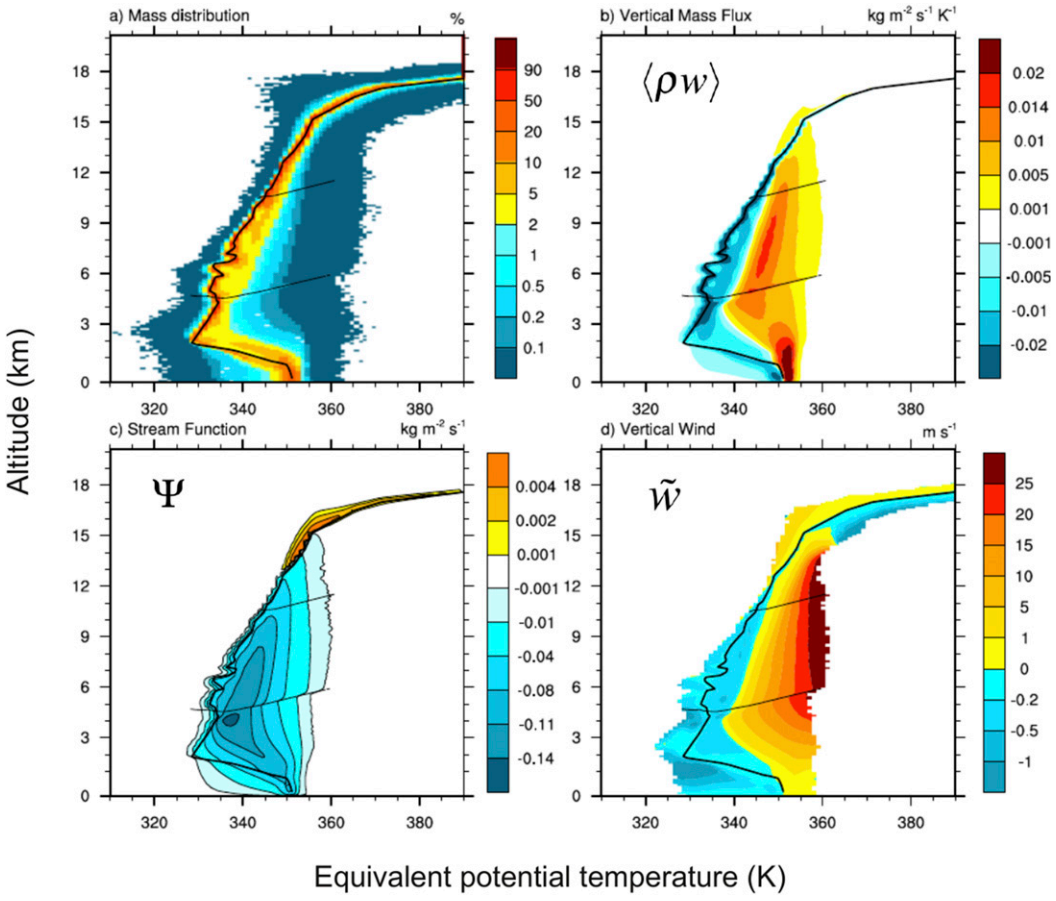

FIG. 2. Isentropic diagrams for the period between 1331 and 1345 LT, during the very deep convective phase. (a) Mass distribution, (b) vertical mass flux, (c) isentropic streamfunction, and (d) bin average of the vertical velocities. The environmental equivalent potential temperature θ_e^{env} profile is represented by the thick black line and the 0° and −38°C isotherms by the thin black lines.

above the freezing level. It represents the downward motion of purely environmental air (compensating subsidence) and of negatively buoyant air that results from the mixing between the cloud edges and the environment (the subsiding shells; e.g., Glenn and Krueger 2014). Below the freezing level, the subsiding branch is tilted toward higher θ_e values because of the mixing with the warmer and/or moister air of the cloud (see Fig. 3e to locate the cloud on the diagram). At the surface, cold pools are generated by the downdrafts with low θ_e.

The second overturning identified by the isentropic streamfunction is the overshoot overturning. Its intensity is $0.005\,\text{kg}\,\text{m}^{-2}\,\text{s}^{-1}$ (1/30 of the tropospheric overturning intensity), and it spans from 13- to 18-km altitudes. At the tropopause (17-km altitude), the maximum of Ψ is $0.0025\,\text{kg}\,\text{m}^{-2}\,\text{s}^{-1}$, indicating that only half of the overshoot overturning is actually crossing the tropopause. The ascending branch of this overturning is at lower θ_e than the environment, down to 10 K less than θ_e^{env}. The subsiding branch follows the θ_e^{env} profile.

b. *Buoyancy and microphysics*

The isentropic analysis also provides a framework to investigate the microphysical properties of the overturnings. The large hydrometeor content and the high buoyancy of the ascending branches are shown for both the tropospheric and the overshoot overturning (Fig. 3).

Above 13 km, the overshoot signature is remarkable, with large negative buoyancy (below $-0.1\,\text{m}\,\text{s}^{-2}$) and large frozen water contents (e.g., more than $2\,\text{g}\,\text{kg}^{-1}$ of graupel content) for air parcels with θ_e several degrees lower than the values of θ_e^{env}. The overshooting air parcels with θ_e close to θ_e^{env} can, however, not be distinguished from the surrounding air parcels by the isentropic analysis, leading to buoyancy close to zero and a much lower ice content on average than the

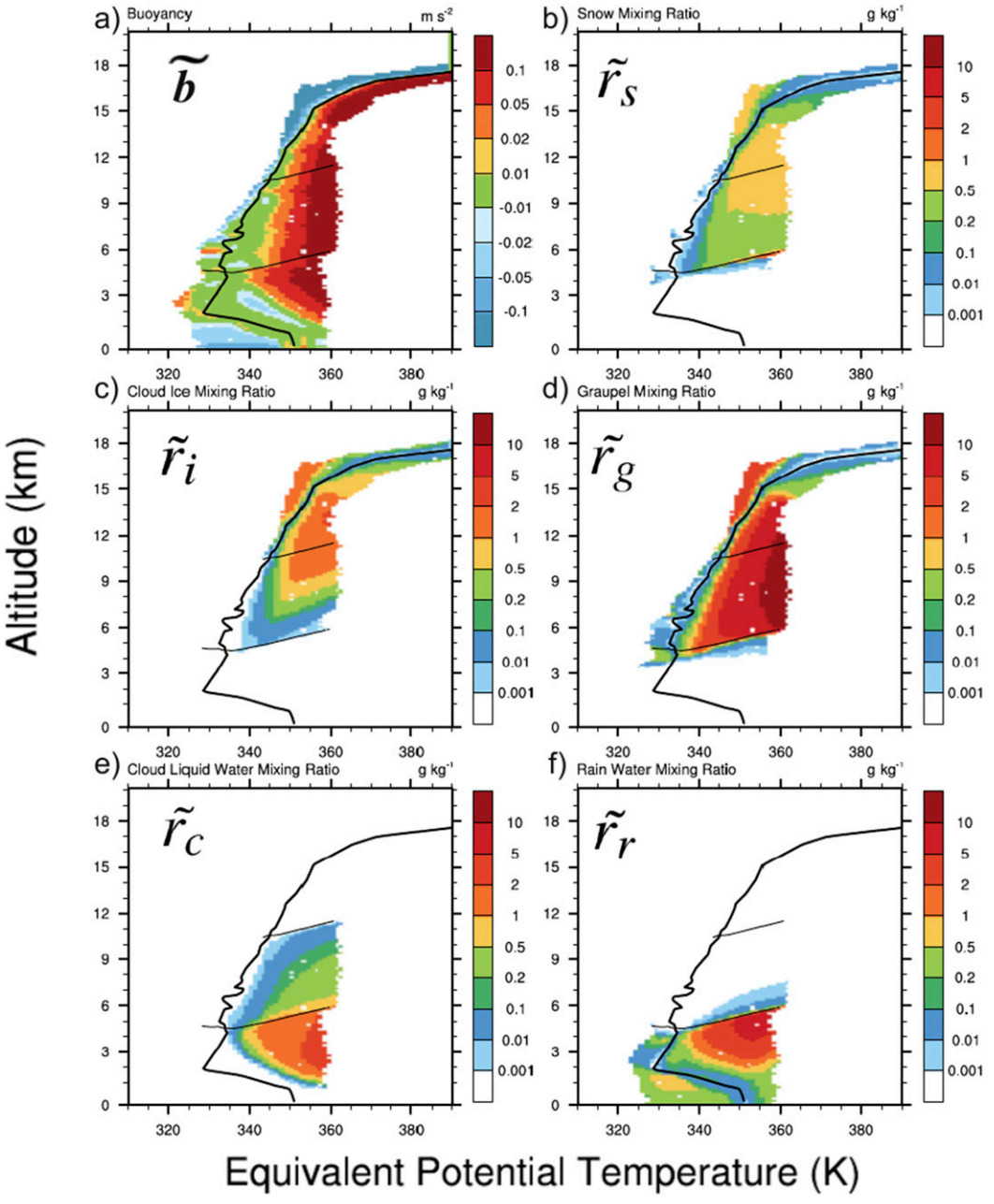

FIG. 3. As in Fig. 2, but for the conditional average of (a) buoyancy, (b) snow, (c) cloud ice, (d) graupel, (e) cloud liquid water, and (f) rain mixing ratios.

overshooting air parcels with θ_e several degrees lower than θ_e^{env}.

Between the 0° and −38°C isotherms, the parcels with θ_e higher than 350 K have large positive buoyancy and a large amount of cloud supercooled liquid water. The supercooled liquid water has been lofted by the strong updrafts seen in Fig. 2d. The rainwater freezes more quickly than the cloud liquid water because of the greater efficiencies of the collection by graupel and snow. The freezing of a large amount of rainwater leads to a large amount of graupel, over $5\,\text{g}\,\text{kg}^{-1}$ for air parcels with θ_e 10 K higher than the environment. Between 7- and 11-km altitudes, the cloud liquid water freezes primarily because of collection by graupel or snow aggregates, two processes that are parameterized in Meso-NH.

Between the surface and 2-km altitude, the air masses with θ_e lower than θ_e^{env} are the signature of the cold

pools. They contain around 0.5 g kg^{-1} of rainwater on average. The ascending branches of both the tropospheric and the overshoot overturnings are characterized by a large absolute value of buoyancy (beyond 0.1 m s^{-2} above 3 km) and large amount of ice (over 10 g kg^{-1}). The ascending branch of the tropospheric overturning exhibits also a large amount of supercooled water (around 0.5 g kg^{-1}) over a large range of altitudes (between 5 and 11 km).

4. Convective regimes

The development of Hector the Convector is strongly tied to the diurnal cycle (Dauhut et al. 2016). In the early morning, the sea breeze generates low-level convergence over the Tiwi Islands and the shallow convection develops. Dauhut et al. (2016) define then four successive phases of convective regime, each phase lasting one hour. The congestus convection phase starts at 1115 LT, the deep convection phase at 1215 LT with the development of the first cumulonimbus, the very deep convection phase at 1315 LT when overshoots begin to reach the lower stratosphere, and the mature convection phase at 1415 LT when the hydrometeor content in the atmosphere is maximum.

a. Stream functions

The four successive phases of convection are investigated using the isentropic streamfunction (Fig. 4). For all the convection phases, the main overturning is constituted by an ascending branch at high θ_e, close to the value at the surface, and a subsiding branch at low θ_e, close to the environment profile θ_e^{env}. The overturnings are characterized by their vertical extent and by their intensity. On the one hand, the tropospheric overturning exhibits a gradual growth of its vertical extent. On the other hand, its intensification is strong, with an intensity 1.5 times larger during the very deep convection phase than during the other phases. In the TTL, the 0.005 kg m^{-2} s^{-1} overturning during the very deep convection phase shrinks into an overshoot overturning that does not reach altitudes higher than 15 km, well below the tropopause. The very deep convection phase stands out within all the phases, with the intensity of the tropospheric overturning and of the overshoot overturning much larger than during the other phases, in agreement with the evolution of the vertical mass flux given by Dauhut et al. (2016) for their giga-LES of Hector.

While the streamfunction is typically negative through most of the atmosphere—corresponding to the ascent of warm, moist air and subsidence of cooler, drier air parcels—small regions of positive values of the streamfunction can be identified during different stages of Hector the Convector. The positive values of the streamfunction are about 30 times smaller than the negative ones. During both the very deep convection and the mature convection phases, positive values of the streamfunction are found in the upper troposphere. This indicates the presence of convective overshoot, as the equivalent potential temperature of the rising air parcels is less than that of the descending air. In addition, we also observe positive values of the streamfunction in the lower troposphere during the congestus and mature convection phases. In both phases, air with very low θ_e (about 330 K) rises. Such air parcels would be negatively buoyant and could only rise if mechanically forced. From a physical point of view, we associate this behavior with the entrainment of low-θ_e environmental air into cumulus clouds.

The streamlines can be interpreted piecewise as the Lagrangian paths followed on average by the air parcels. Their slope gives an indication of the average trend in θ_e along the air parcels' motion. From the congestus phase (Fig. 4a) to the very deep convection phase (Fig. 4c), the ascending branch of the circulation is gradually less tilted toward the θ_e^{env} profile, suggesting a decreasing loss of θ_e for the rising air parcels. Below the freezing level, the slopes of the streamlines are explained by the variations in θ_e due to mixing. Rising air parcels lose θ_e as they mix with lower θ_e air from the environment. As the convection develops from the congestus phase to the very deep phase, the steepening of the streamlines shows the gradual reduction of the mixing. The upright streamlines during the very deep convection phase suggest an extremely low mixing for some rising air parcels.

Above the freezing level, ice formation is a source of θ_e. The deposition of water vapor on cloud ice is the ice process that contributes the most to the release of latent heat. In the 1-km-deep layer above the freezing level, the air parcels experience a mean increase of θ_e as they ascend. Such a trend, despite the mixing, indicates a large latent heat release due to ice formation. Above this shallow layer and up to the top of the tropospheric overturning, the streamlines are tilted toward low θ_e values during the deep convection phase, become upright, and eventually are tilted toward large θ_e values during the very deep and the mature convection phases. This change of slope with time is associated with an increasing amount of latent heat release due to ice formation. The intensity of the latent heat release is further illustrated in terms of average θ tendencies (Fig. 5). The θ tendencies due to microphysics dominate the ones due to radiation and turbulence; they are partly balanced by the advection. The diabatic tendencies due to radiation are positive and important in the uppermost part of the

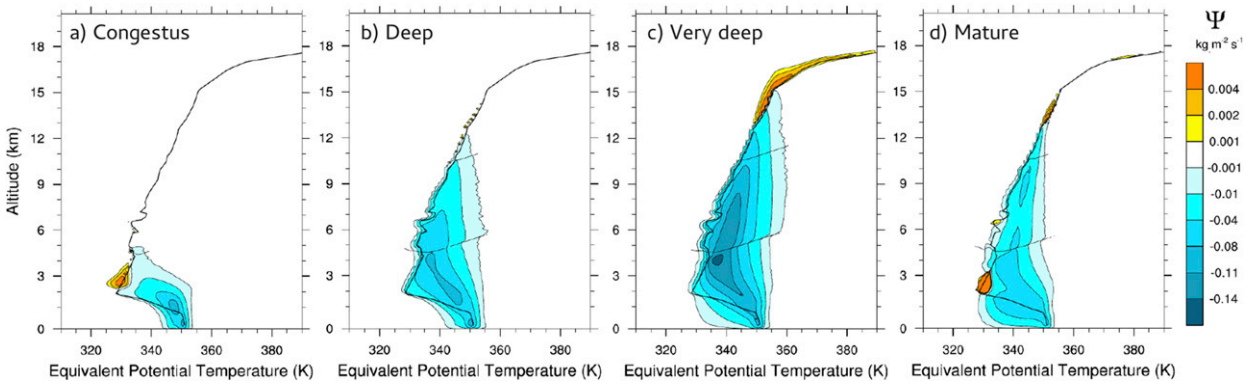

FIG. 4. The streamfunctions for (a) 1131–1145 LT during the congestus convection phase, (b) 1231–1245 LT during the deep convection phase, (c) 1331–1345 LT during the very deep convection phase, and (d) 1431–1445 LT during the mature convection phase. The black lines are as in Fig. 2.

cloud only (between 12- and 18-km altitudes, where the cloud is made of ice only). These positive tendencies might be due to the fact that the anvil absorbs more longwave radiation from the ground than it emits. Note that this positive tendency balances the negative one because of the ice sublimation in the uppermost part of the cloud during the very deep convection phase.

A reduction of the mixing experienced by the ascending air parcels could also contribute to this change of slope above the freezing level. A method to disentangle the dilution from the latent heat release due to ice formation consists in using another isentropic coordinate. Along with θ_e, liquid moist static energy ξ_l, which is insensitive to any latent heat change (but sensitive to liquid precipitation), is used as an alternative isentropic coordinate in the following sections in order to investigate the dilution of the updrafts above the freezing level.

b. Diabatic tendencies

Pauluis and Mrowiec (2013) show that, for an atmosphere in radiative–convective equilibrium, the diabatic

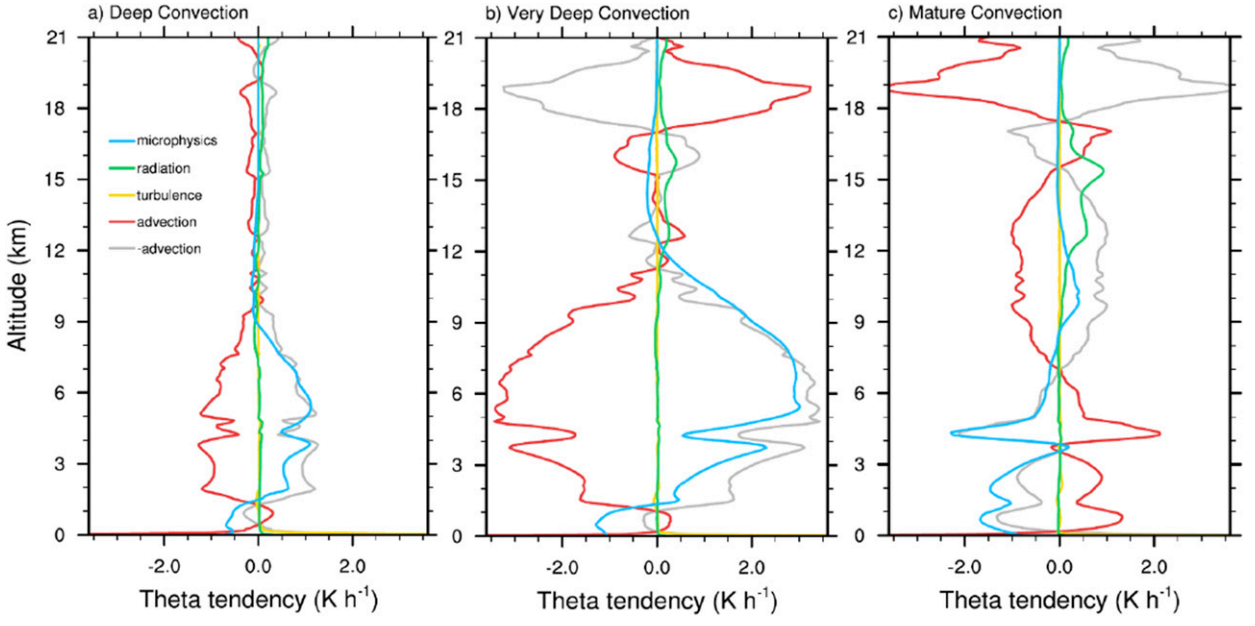

FIG. 5. Vertical profiles of the tendencies of θ due to microphysics, turbulence, radiation, and advection, averaged over the domain of the isentropic analysis (Fig. 1) during the same time periods as in Figs. 4b–d: during the (a) deep convection phase, (b) very deep convection phase, and (c) mature convection phase. The opposite of the tendency due to advection is superimposed in gray for an easier comparison with the one due to microphysics.

tendencies are equal to the vertical derivative of the streamfunction $\langle \rho \dot{\theta}_e \rangle = -\partial/\partial z \Psi$. This result, however, is only valid for an atmosphere in statistical equilibrium and in a domain with periodic lateral boundary conditions. In the Hector simulation, the modeled atmosphere is evolving over time and continuously exchanges air at its lateral boundary. We show in the appendix how to account for the lateral boundary conditions and time evolution to retrieve the diabatic tendency.

The retrieved diabatic tendencies during the four different stages of Hector the Convector are shown in Fig. 6. Below the freezing level, the diabatic tendencies show a clear dipole during all phases. In this part of the atmosphere, the mixing is the most important diabatic process that can alter θ_e. The latent heat absorption due to melting of ice leads to significant negative tendencies only in a narrow band of altitudes below the freezing level (Figs. 6c,d; visible as a marked, local minimum of the θ tendency due to microphysics in Fig. 5). The line (not plotted) going from 350 K at the surface to 342 K at 4 km delimits lower-θ_e air parcels with positive tendency and higher-θ_e air parcels with negative tendency. On the one hand, the air parcels with high θ_e are part of the updrafts that are cooled down and/or dried by the mixing with the surrounding air. On the other hand, the air parcels with θ_e closer to θ_e^{env} are warmed up and/or moistened by this mixing.

Above the freezing level and below the −38°C isotherm (Fig. 6), air parcels with θ_e larger than 344 K show a radical change in diabatic tendencies between the deep and very deep convection phases (Figs. 6b,c): from negative to positive. The latent heat release due to ice formation is the positive contribution to the diabatic tendencies with θ_e, and it exceeds the negative diabatic tendencies due to the mixing since the diabatic tendencies with θ_e are positive. The large latent heat release noticed in the (z, θ_e) space is also evidenced when examining the averaged profiles of θ tendency (Fig. 5). The tendency due to microphysics slightly exceeds the advection tendency between 7.5- and 12-km altitudes during the very deep convection phase only. During the congestus phase, it is 3 times smaller. During the mature phase, it becomes even negative because of melting and evaporation of stratiform precipitation. The details of the microphysical processes indicate that the deposition of vapor onto the icy hydrometeors is the most important source of latent heat. The amount of graupel (with mixing ratio up to 10 g kg^{-1}; see Fig. 3) increases because of the intense accretion of rain with snow and the collection of snow, cloud ice, and cloud water by the preexisting graupel particles between 4.5- and 8-km altitudes. These results depend strongly on the microphysical scheme. More sophisticated schemes, such as the two-moment ones, should give different answers to the importance of each microphysical process and different heating profiles (e.g., Lebo et al. 2012; Grabowski and Jarecka 2015). The air parcels with θ_e larger than 344 K and between 5- and 10-km altitudes are visualized in the physical space in Fig. 7, around the tallest updrafts identified by Dauhut et al. (2016). The increasing volume of air exceeding $\theta_e = 344$ K reveals the warming and moistening of the free troposphere by the convective activity. Above the −38°C isotherm (Fig. 6c), the mixing between the updrafts and the environment warms the environment below 13-km altitude and warms the updrafts above.

In the θ_e framework, the mixing cannot be differentiated from the ice formation. Then the entrainment cannot be retrieved from the diabatic tendencies above the freezing level. To separate the ice formation from the mixing, we further use the liquid moist static energy ξ_l as isentropic coordinate. The same approach as with θ_e can be used to retrieved the diabatic tendencies in the ξ_l framework. The liquid moist static energy is defined in temperature units:

$$\xi_l = T + \frac{g}{C_{\text{pd}}} z + \frac{L_s}{C_{\text{pd}}} r_v + \frac{L_f}{C_{\text{pd}}} (r_c + r_r), \tag{5}$$

where g is the acceleration of the gravity, L_s is the latent heat of sublimation, and r_c and r_r are the mixing ratio of cloud liquid water and rain, respectively. The liquid moist static energy is conserved under ice formation but not in case of liquid precipitation. It is worth noting that the positive contribution from the formation of ice in the θ_e framework is replaced by a negative contribution in ξ_l tendency associated with the loss of liquid water by precipitation. The air parcels concerned by this nonconservation are mostly located below the freezing level (see Fig. 3f). Above the freezing level, the large diabatic term seen with θ_e disappears and is replaced by a mostly negative tendency (Figs. 8b–d), indicating that entrainment is still active.

c. *Entrainment*

Entrainment is the incorporation of environmental air into a rising plume. Considering the updrafts, the entrainment rate ε quantifies their dilution by mixing with the surrounding air masses. Any property ϕ that is conserved in absence of dilution can be used to compute ε. In the bulk formulation, the entrainment rate is the factor that scales the decrease with height of the conserved property inside the updraft with the difference of the environmental value [first two members of Eq. (6)]. In the frame of the isentropic analysis, the entrainment rate ε is deduced from Eq. (6) as the ratio between the

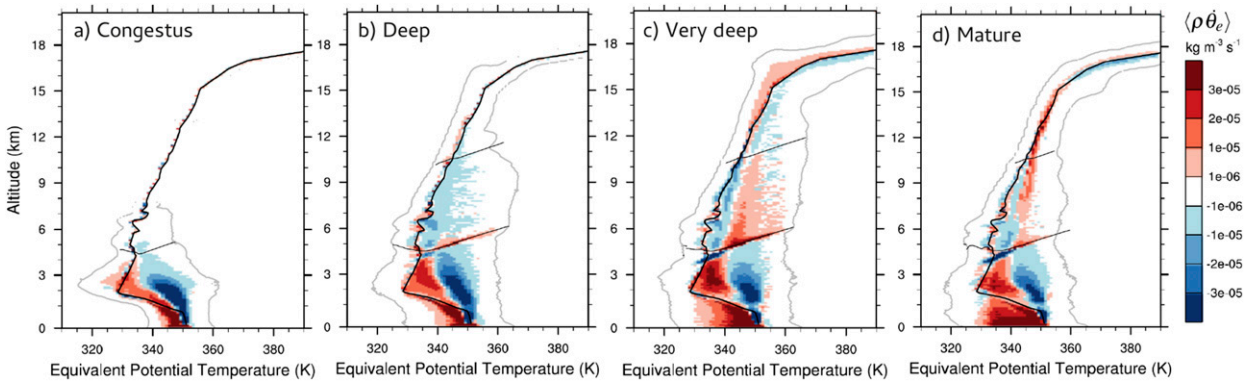

FIG. 6. As in Fig. 4, but for diabatic tendencies with θ_e as the isentropic coordinate. The envelope of the mass distributions of each period is shown with the gray lines.

diabatic tendency and the vertical mass flux times the difference of ϕ with the environment. Although the rising air parcels can mix with each other, the environmental profile ϕ^{env} is here the constant profile at the boundaries of the domain. This choice leads to values of ε that can be read as an effective entrainment rate. It allows easier comparison with the entrainment rates in other paradigms:

$$\varepsilon(\phi^{\text{env}} - \phi) = \frac{\widetilde{\dot{\phi}}}{\tilde{w}} = \frac{\langle \rho \dot{\phi} \rangle}{\langle \rho w \rangle}. \tag{6}$$

The conserved properties used here are θ_e below the freezing level (Figs. 9e–h) and ξ_l above (Figs. 9a–d). These properties are virtually conserved in absence of dilution in two distinct regions. Below the freezing level, the rate of change of θ_e due to mixing dominates the sinks and sources because of radiation (by at least one order of magnitude) and the ones due to ice formation (negligible below the freezing level). The error in ε due to ice melting is negligible (less than $0.02\,\text{km}^{-1}$) at low ice concentration (below the purple line in Figs. 9e–h). Above the freezing level, the rate of change of ξ_l due to mixing dominates the sinks and sources because of radiation and to liquid water precipitation. The error in ε assuming that all supercooled rain falls out is negligible (less than $0.02\,\text{km}^{-1}$) at low rain concentration (above the purple line in Figs. 9a–d).

The entrainment rate is shown for the successive convection phases in Fig. 9. Given the limits of the bulk model for the entrainment (de Rooy et al. 2013), only the bins where $\tilde{w}$ and ε are positive are shown. The entrainment rate ε during the congestus phase (Figs. 9a,e) contrasts from ε during the three next phases, with values exceeding $0.2\,\text{km}^{-1}$ almost everywhere. From the deep convection phase onward (Figs. 9b–d,f–h), values of entrainment as low as $0.04\,\text{km}^{-1}$ are found. During the deep convection phase, such low ε is found for air parcels with very high θ_e or ξ_l only, below 7-km altitude. The minimum of ε is reached during the very deep

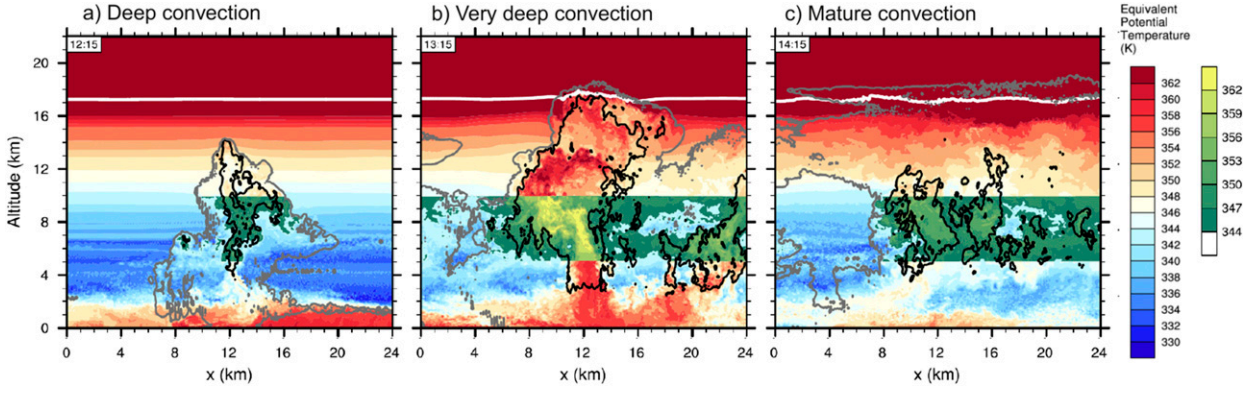

FIG. 7. Vertical cross sections of the tallest updrafts studied by Dauhut et al. (2016) at (a) 1215, (b) 1315, and (c) 1415 LT. The color shading is θ_e, the black contours are the updrafts with a vertical velocity exceeding $10\,\text{m s}^{-1}$, and the gray contour is the cloud envelope. Yellow–green shadings overlay air parcels between 5- and 10-km altitudes and with θ_e over 344 K.

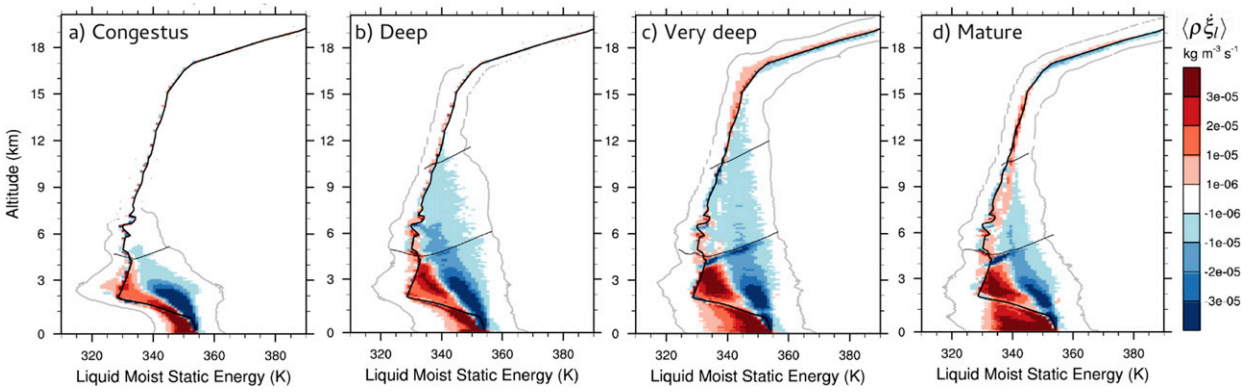

FIG. 8. As in Fig. 6, but with ξ_l as the isentropic coordinate.

convection phase, when values of ε lower than 0.06 km^{-1} are associated with many rising air parcels up to the −38°C isotherm. After, during the mature convection phase (Figs. 9d,h), the entrainment rate returns to values about 0.1 km^{-1}. For all phases, the computation of ε in the overshoot regions leads to large values, over 1 km^{-1}.

The computation of ε exhibits a strong decrease in the updrafts' dilution between the congestus and the very deep convection phase. The extremely low entrainment rates during the very deep convection phases (lower than 0.04 km^{-1}) confirm and even break the very low values found for the tallest updrafts of Hector [down to 0.08 km^{-1} in Dauhut et al. (2016)]. The occurrence of the minimal entrainment in the troposphere found for some individual updrafts during the very deep convection phase is thus confirmed at the scale of the multicellular convective system Hector.

5. Mass transport

The mass transport toward the stratosphere by Hector on 30 November 2005 was quantified by Dauhut et al. (2016), who showed the vertical profiles of the airmass transports for the very deep convection phase (Fig. 10a, the blue profile). This study took into account the contribution of the updrafts, where the vertical velocity

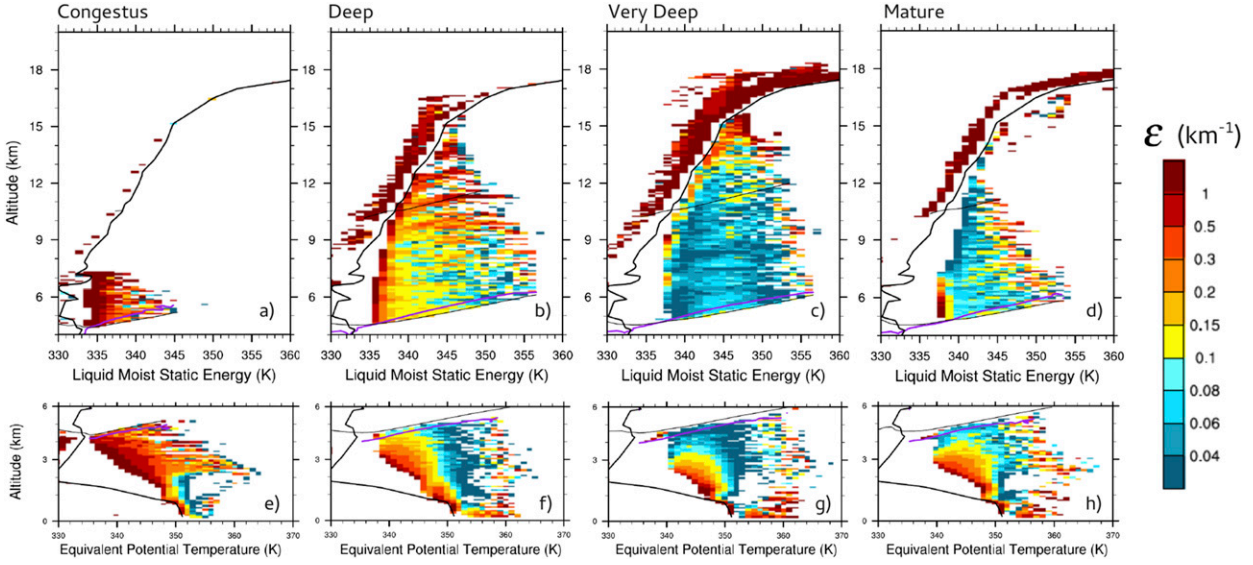

FIG. 9. The entrainment rate for the same time periods as in Fig. 4: during the (a),(e) congestus convection phase, (b),(f) deep convection phase, (c),(g) very deep convection phase, and (d),(h) mature convection phase. (top) Values above the freezing level computed with ξ_l as the isentropic coordinate; above the purple line, the error in ε due to liquid precipitation is less than 0.02 km^{-1}. (bottom) Values below the freezing level computed with θ_e as the isentropic coordinate; below the purple line, the error in ε due to ice processes is less than 0.02 km^{-1}. The black lines are as in Fig. 2. The wide white areas without entrainment values correspond to bins where $\tilde{w}$ or ε is negative.

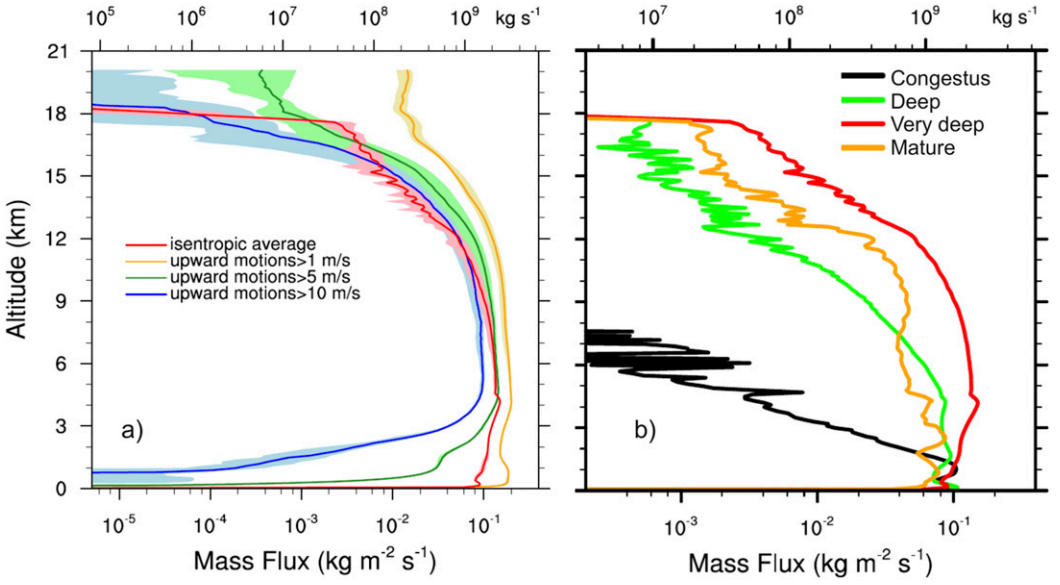

FIG. 10. (a) Vertical mass flux computed by the isentropic analysis between 1331 and 1345 LT (red), compared to the transport due to all the upward motions stronger than 1 (yellow), 5 (green), and 10 m s^{-1} (blue). The thick lines show the averaged values, while the color shades span between the minimum and maximum values taken during each 15-min period. (b) Averaged vertical mass flux computed by the isentropic analysis for the same time periods as in Fig. 4: during the congestus convection phase (black), deep convection phase (green), very deep convection phase (red), and mature convection phase (orange). The scale at the top gives the total vertical mass flux over the area of the analysis domain: 1.6×10^{10} m^2.

exceeds 10 m s^{-1}, in order to exclude the reversible transport due to gravity waves. The isentropic analysis offers the possibility to quantify the transport with a radically different method. Neither coherent structure needs to be detected, nor do any arbitrary thresholds need to be defined. Furthermore, the isentropic quantification of the transport takes into account the transport by highly transient, incoherent, and turbulent eddies. The subsequent quantification is compared with the former Eulerian computations that take into account the transport by motions stronger than some threshold only and that do not necessarily exclude all of the reversible mass transport.

The mass transport is defined here following Pauluis and Mrowiec (2013). It can be derived from the isentropic streamfunction Ψ as the difference between its maximum and its minimum, at each level. The time variability is estimated with the quantification from the every minute output. The isentropic mass transport during the very deep convection phase (Fig. 10a, the red profile) peaks just below the freezing level, at 4-km altitude, in contrast with the mass transport computed for the radiative–convective equilibrium simulation of Pauluis and Mrowiec (2013), which peaks in the lower part of the boundary layer, at about 300-m altitude. For a mesoscale convective system, Mrowiec et al. (2015) find a maximal vertical mass transport close to the freezing level. This location of the maximum further confirms that ice formation acts as a buoyancy kick that changes the dynamical behavior of the updrafts, from mostly entraining below to mostly detraining above. The mass transport decreases in a quadratic way with height up to 12-km altitude, and decays exponentially above, with a scale height of 4 km. The isentropic mass transport is compared to the Eulerian mass transport, computed with thresholds on the vertical velocities. On the one hand, the use of a low velocity threshold (1 m s^{-1}) systematically overestimates the mass transport everywhere, as it tends to include too much of the mass transport. On the other hand, the larger velocity thresholds miss most of the mass transport in the lower troposphere. When compared with the isentropic mass transport, the 10 m s^{-1} threshold leads to a reasonable quantification of the vertical mass flux between 10- and 16-km altitudes. This result is consistent with the strong average vertical velocities $\tilde{w}$ in the upper troposphere (Fig. 2d). The use of these large thresholds, however, tends to underestimate the isentropic mass flux near the tropopause. This highlights the significative contribution of the small-amplitude motions to the cross-tropopause transport.

The comparison of the irreversible upward mass fluxes for the successive convection phases is shown in Fig. 10b. The congestus phase contrasts from the three later phases with a mass flux that drops sharply with altitude, from 2-km altitude upward. Large variations

of the mass flux profiles with altitude are observed between 13- and 17-km altitudes for the deeper convection phases. These variations might be caused by the fact that the updrafts and the environment have similar values for θ_e in these ranges of altitudes. In agreement with the Eulerian computation (Dauhut et al. 2016), the upward mass flux increases from the deep to the very deep convection phase and decreases back during the mature convection phase. At the tropopause (17-km altitude), the 3.5 10^{-3} kg m^{-2} s^{-1} upward mass fluxes during the very deep convection phase drop by a factor of 2.6 one hour later. These fluctuations highlight the transient nature of the cross-tropopause transport by convection and the difficulty in observing it.

6. Conclusions

A large-eddy simulation (200-m horizontal grid spacing and 1-min time resolution) performed by Dauhut et al. (2015) has been used to quantify the irreversible mass flux across the troposphere by Hector the Convector on 30 November 2005. The isentropic analysis filters out the buoyant oscillations by averaging the contribution of thermodynamically similar air parcels and takes into account the mass flux due to small-amplitude motions thanks to the absence of a threshold. Two key circulations due to Hector have been characterized by the isentropic streamfunction.

The tropospheric overturning transports energetic air parcels from the surface to their level of neutral buoyancy and less energetic air parcels, thermodynamically similar to the environment, from the upper troposphere to the surface. The intensity of the tropospheric overturning is about 0.1 kg m^{-2} s^{-1} from the congestus convection phase to the mature convection phase, except during the very deep convection phase when its intensity increases to 0.15 kg m^{-2} s^{-1}. As shown by Dauhut et al. (2016), the updrafts contribute significantly to the upward mass transport while the downdrafts temper this upward mass transport, especially in the upper troposphere and just below the freezing level.

The overshoot overturning transports upward air parcels beyond their level of neutral buoyancy. It extends up to 18 km during the very deep convection phase, whereas it splits into two circulations that are separated by the tropopause during the mature convection phase.

The irreversible mass transport computed by the isentropic analysis is about 10^{-1} kg m^{-2} s^{-1} from the surface up to 11-km altitude. Above 11-km altitude, the mass flux decreases exponentially with altitude, down to 3.5×10^{-3} kg m^{-2} s^{-1} at 17-km altitude (the tropopause). It drops to zero just above 18-km altitude. The isentropic mass flux computation is compared to the Eulerian computations that use 10 and 5 m s^{-1} thresholds on the vertical velocity field. The isentropic estimate is one order of magnitude larger than the Eulerian ones at the tropopause and in the lower troposphere. This difference is attributed to the contribution of the small-amplitude motions. In contrast, the isentropic estimate of the mass flux is slightly lower than the Eulerian estimates between 13- and 15-km altitudes. The estimates are in the range of the temporal variability of one another. The larger estimates of the Eulerian approach are attributed to the reversible motions like gravity waves, which actually do not transport mass. Mrowiec et al. (2015) compare the Eulerian and isentropic computations of the vertical mass flux for another deep convective event around Darwin. The Eulerian computation based on a positive velocity threshold gives a 50% larger estimate than the isentropic computation. The maximum of the isentropic vertical profile occurs just below the freezing level, like in this study. Its value (0.06 kg m^{-2} s^{-1}) is, however, lower than the maximum of the deep and mature convection profiles of Hector.

The isentropic analysis also allows us to retrieve the diabatic tendencies and to interpret them in the light of the heating rates due to microphysics, turbulence, and radiation, averaged at the system scale. The mixing of the air parcels with their surrounding environment is distinguished from the latent heat release by the use of two different isentropic coordinates. The entrainment rate is then quantified using the estimate of the mixing. The entrainment rate exhibits a minimum during the very deep convection phase, with values as low as 0.04 km^{-1} for many air parcels between 1- and 11-km altitudes. The isentropic analysis confirms the existence of weakly diluted air parcels, especially during the very deep convection phase. This entrainment rate stands in contrast with the values down to 0.25 km^{-1} found for deep convection up to 12-km altitude over ocean (Kuang and Bretherton 2006) and down to 0.1 km^{-1} for deep convection reaching 14-km altitude over Amazonia (Khairoutdinov and Randall 2006).

The diabatic tendencies further reveal a change in regime between the deep and the very deep convection phases. During the very deep convection phase, the positive tendency by latent heating due to ice processes exceeds the negative tendency because of the mixing of the rising air parcels with the surrounding air. In contrast, during the deep convection phase, such large contribution of the latent heat release is confined to the vicinity of the freezing level. The sensitivity of the diabatic tendencies to the microphysical scheme needs though to be further investigated, and the isentropic analysis provides a convenient frame for such an intercomparison.

Acknowledgments. This research was supported by the StratoClim project funded by the European Union Seventh Framework Programme under Grant Agreement 603557. Computer resources were allocated by GENCI through Projects 90569 and 100231 (Grand Challenge Turing). Olivier Pauluis is supported by the New York University Abu Dhabi Research Institute under Grant G1102.Turing. We thank the editor and the anonymous referees for their comments, which helped to improve the overall quality of the paper.

APPENDIX

Reconstruction of Diabatic Tendencies

Pauluis and Mrowiec (2013) have shown that for radiative convective equilibrium, the diabatic tendency $\dot{\theta}_e$ can be directly inferred from the isentropic streamfunction, with

$$\frac{\partial \langle \rho w \rangle}{\partial z_0} + \frac{\partial \langle \rho \dot{\theta}_e \rangle}{\partial \theta_{e0}} = 0. \tag{A1}$$

However, this result only holds for a close atmosphere in statistical equilibrium. In our study, however, both conditions are violated, as our simulation allows for open boundaries, and the atmosphere is evolving rapidly. It is, however, possible to retrieve the diabatic tendencies in this case as well. The continuity equation is then given by

$$\frac{\partial \langle \rho \rangle}{\partial t} = \mathcal{F}_{\text{lat}} - \frac{\partial \langle \rho w \rangle}{\partial z_0} - \frac{\partial \langle \rho \dot{\theta}_e \rangle}{\partial \theta_{e0}}. \tag{A2}$$

The first term on the RHS $\mathcal{F}_{\text{lat}}$ is the source term because of the advection of air in and out of the analysis domain. The term on the LHS and the first two terms of the RHS are directly computed from the output of the model. The computation of the last term as a residue allows us to quantify the effect of the diabatic processes on the mass distribution.

REFERENCES

Chaboureau, J.-P., J.-P. Cammas, J. Duron, P. J. Mascart, N. M. Sitnikov, and H.-J. Voessing, 2007: A numerical study of tropical cross-tropopause transport by convective overshoots. *Atmos. Chem. Phys.*, **7**, 1731–1740, doi:10.5194/acp-7-1731-2007.

Dauhut, T., J.-P. Chaboureau, J. Escobar, and P. Mascart, 2015: Large-eddy simulation of Hector the Convector making the stratosphere wetter. *Atmos. Sci. Lett.*, **16**, 135–140, doi:10.1002/asl2.534.

——, ——, ——, and ——, 2016: Giga-LES of Hector the Convector and its two tallest updrafts up to the stratosphere. *J. Atmos. Sci.*, **73**, 5041–5060, doi:10.1175/JAS-D-16-0083.1.

de Rooy, W. C., and Coauthors, 2013: Entrainment and detrainment in cumulus convection: An overview. *Quart. J. Roy. Meteor. Soc.*, **139**, 1–19, doi:10.1002/qj.1959.

Dessler, A. E., 2002: The effect of deep, tropical convection on the tropical tropopause layer. *J. Geophys. Res.*, **107**, 4033, doi:10.1029/2001JD000511.

Emanuel, K. A., 1994: *Atmospheric Convection.* Oxford University Press, 580 pp.

Gettelman, A., M. L. Salby, and F. Sassi, 2002: Distribution and influence of convection in the tropical tropopause region. *J. Geophys. Res.*, **107**, 4080, doi:10.1029/2001JD001048.

Glenn, I. B., and S. K. Krueger, 2014: Downdrafts in the near cloud environment of deep convective updrafts. *J. Adv. Model. Earth Syst.*, **6**, 1–8, doi:10.1002/2013MS000261.

Grabowski, W. W., and D. Jarecka, 2015: Modeling condensation in shallow nonprecipitating convection. *J. Atmos. Sci.*, **72**, 4661–4679, doi:10.1175/JAS-D-15-0091.1.

Khairoutdinov, M. F., and D. A. Randall, 2006: High-resolution simulation of shallow-to-deep convection transition over land. *J. Atmos. Sci.*, **63**, 3421–3436, doi:10.1175/JAS3810.1.

Kuang, Z., and C. S. Bretherton, 2006: A mass-flux scheme view of a high-resolution simulation of a transition from shallow to deep cumulus convection. *J. Atmos. Sci.*, **63**, 1895–1909, doi:10.1175/JAS3723.1.

Küpper, C., J. Thuburn, G. C. Craig, and T. Birner, 2004:Mass and water transport into the tropical stratosphere: A cloud-resolving simulation. *J. Geophys. Res.*, **109**, D10111, doi:10.1029/2004JD004541.

Lafore, J.-P., and Coauthors, 1998: The Meso-NH atmospheric simulation system. Part I: Adiabatic formulation and control simulations. *Ann. Geophys.*, **16**, 90–109, doi:10.1007/s00585-997-0090-6.

Lebo, Z. J., H. Morrison, and J. H. Seinfeld, 2012: Are simulated aerosol-induced effects on deep convective clouds strongly dependent on saturation adjustment? *Atmos. Chem. Phys.*, **12**, 9941–9964, doi:10.5194/acp-12-9941-2012.

Liu, C., and E. J. Zipser, 2005: Global distribution of convection penetrating the tropical tropopause. *J. Geophys. Res.*, **110**, D23104, doi:10.1029/2005JD006063.

Mrowiec, A. A., O. M. Pauluis, A. M. Fridlind, and A. S. Ackerman, 2015: Properties of a mesoscale convective system in the context of an isentropic analysis. *J. Atmos. Sci.*, **72**, 1945–1962, doi:10.1175/JAS-D-14-0139.1.

Pauluis, O. M., and A. A. Mrowiec, 2013: Isentropic analysis of convective motions. *J. Atmos. Sci.*, **70**, 3673–3688, doi:10.1175/JAS-D-12-0205.1.